JⱮM PAPERS

Effects of the geothermal gradient on the convective dissolution in CO_2 sequestration

Chenglong Hu[1,2], Ke Xu[3] and Yantao Yang[1,2],†

[1]State Key Laboratory for Turbulence and Complex Systems and Department of Mechanics and Engineering Science, College of Engineering, Peking University, Beijing 100871, P.R. China

[2]Joint Laboratory of Marine Hydrodynamics and Ocean Engineering, Laoshan Laboratory, Shandong 266299, P.R. China

[3]Department of Energy and Resources Engineering, College of Engineering, Peking University, Beijing 100871, P.R. China

Convective dissolution is an important mechanism for long-term CO_2 sequestration in deep saline aquifers. The presence of an unstable geothermal gradient can affect the process of dissolution. In this paper, we present direct numerical simulations in a three-dimensional porous medium at three different concentration Rayleigh numbers Ra_S with a set of thermal Rayleigh numbers Ra_T. Simulations reveal that the flow structures alter when Ra_T increases for a fixed Ra_S. Strong thermal gradient can yield large-scale convection rolls which change the horizontal distribution and motions of concentration fingers. The time evolution of fluxes also has different responses to different Ra_T. A theoretical model is developed and successfully describes the evolution of concentration flux and volume averaged concentration during the final shutdown stage. We further calculate the dissolved CO_2 into the interior over time, which shows non-monotonic variations as Ra_T increases. At the end of our simulations, the maximum increment of dissolved CO_2 occurs when density ratio is around unity for all three concentration Rayleigh numbers we have explored. We apply our results to a typical geological reservoir and discuss their implications.

Key words: convection in porous media, turbulent convection

1. Introduction

In response to the climate change, it is crucial to control and reduce the carbon dioxide (CO_2) emission by human activities, as well as to capture and store the atmospheric carbon dioxide (Orr 2009; Emami-Meybodi *et al.* 2015). Among various strategies, one of the

† Email address for correspondence: yantao.yang@pku.edu.cn

most practical and promising methods is to inject the captured CO_2 into suitable saline aquifers deep underground, as such environments are estimated to exhibit considerable capacity for CO_2 storage (Orr 2009). At surface atmospheric conditions, CO_2 is in a stable gas state. While being injected into deep saline aquifers at typical depths between 800 and 3000 m, CO_2 shifts into the supercritical state due to the high temperature and pressure, which are both above the corresponding values of the critical point (with $T_c = 31.1\,^\circ$C, $P_c = 7.38$ MPa) (Emami-Meybodi *et al.* 2015). The supercritical CO_2 behaves as a liquid with a density more than 150 kg m^{-3} (Bachu 2003).

The supercritical CO_2 is usually injected into saline aquifers below cap rocks which prevent the CO_2 from escaping. The migration of CO_2 is controlled by the differences in density and other thermodynamic properties between the liquid CO_2 and the brine. Huppert & Neufeld (2014) nicely reviewed the fluid mechanics related to underground carbon dioxide sequestration, such as buoyancy-driven propagation, containment and leakage, capillary trapping and convective dissolution. Since the supercritical CO_2 has a smaller density than brine, it will rise and accumulate beneath the cap rock. The CO_2 dissolves into the brine through the interface with the brine below. The brine that is saturated with dissolved CO_2 increases in density and buoyancy-driven convective motions develop under the influence of gravity. This process is convective dissolution, which has been considered as an important mechanism for accelerating mixing and therefore favouring stable long-term storage (Ennis-King & Paterson 2003; Xu, Chen & Zhang 2006; Neufeld *et al.* 2010).

While in experiments it is relatively convenient to include both the supercritical CO_2 layer and the brine layer (Kneafsey & Pruess 2010; Neufeld *et al.* 2010), in numerical simulations the dissolution process at the interface is complicated. A commonly used model configuration for convective dissolution in simulations is a layer of porous medium filled with brine bounded from top and bottom. At the top boundary it is assumed that the brine is saturated by dissolved CO_2 with fixed concentration and higher density. In other words, the top boundary can be treated as a flat and stationary interface between the liquid supercritical CO_2 and pure brine. While at the bottom boundary the no-flux boundary condition is used, so that no dissolved CO_2 is transferred through the bottom boundary. Linear stability analyses have been carried out to investigate the onset of convection, such as the critical time of onset and the critical wavelength of developed fingers (Ennis-King & Paterson 2003; Riaz *et al.* 2006; Xu *et al.* 2006; Chan Kim & Kyun Choi 2012; Myint, Bestehorn & Firoozabadi 2012). The influences of the anisotropic permeability on the linear instability have also been studied (Ennis-King & Paterson 2003; Xu *et al.* 2006; Myint *et al.* 2012; Green & Ennis-King 2018). Two-dimensional (2-D) and three-dimensional (3-D) simulations are conducted to compare with the theoretical predictions of the linear stability analysis, and to reveal the flow developments after the initial linear growth, such as in Neufeld *et al.* (2010), Pau *et al.* (2010) and Green & Ennis-King (2018). One key response of such a system is the dissolution flux at the top boundary. As the flow develops, the flux goes through the diffusive, the linear-growth, the flux-growth, the merging, the constant-flux and finally the shutdown stages. By using 2-D numerical simulations, Slim (2014) has comprehensively studied each state and analysed the corresponding flux evolution. A similar study was carried out later by De Paoli, Zonta & Soldati (2017) for anisotropic media. Since the dissolved CO_2 will accumulate within the domain due to the no-flux condition at the bottom plate, the buoyancy difference across the domain height decreases. The flow motion will eventually slow down and the system enters a shutdown regime. For the long-term shutdown regime Hewitt, Neufeld & Lister (2013)

proposed a linear relation to describe the non-dimensional downward flux and validated with the results from numerical simulations.

Another configuration is similar to Rayleigh–Bénard convection, in which a constant concentration difference is held between the top and bottom boundaries, and the flow will reach a statistically steady state since the buoyancy driving force has a fixed strength. The strength of the buoyancy force is usually measured by the non-dimensional Rayleigh number Ra. Such a model is usually referred to as Rayleigh–Darcy convection (RDC), and the key question is to understand how the non-dimensional flux behaves as Ra increases. Numerical simulations have been conducted for RDC and recently have been pushed to very high Ra. Otero *et al.* (2004) observed a power law $Nu \sim Ra^{0.9}$ in a high-Ra range up to $Ra = 10^4$. Hewitt, Neufeld & Lister (2014) fitted the numerical results more accurately with a linear form $Nu = 0.0096Ra + 4.6$ in the range $1750 \leq Ra \leq 2 \times 10^4$. Pirozzoli *et al.* (2021) further pushed Rayleigh number up to $Ra = 8 \times 10^4$ and obtained a scaling law of $Nu = 0.0081Ra + 0.067Ra^{0.61}$, which predicts the asymptotic linear law towards the ultimate regime.

It should be noted, however, that the background temperature is not always uniform in saline aquifers and the geothermal gradient along the vertical direction is commonly presented. The magnitude of the vertical geothermal gradient has a typical value of $25\,^\circ\mathrm{C\,km^{-1}}$ for the so-called 'cold basins' and can be as high as $50\,^\circ\mathrm{C\,km^{-1}}$ for the 'warm basins' (Bachu 2003; Nordbotten, Celia & Bachu 2005). Rao *et al.* (2001) estimated that the geothermal gradient along the Western Continental Margin of India is in the range of 35–$65\,^\circ\mathrm{C\,km^{-1}}$. When the geothermal gradient is strong enough, the temperature field alone can drive the convective motions. The convective dissolution of CO_2 in saline aquifers with geothermal gradients can be different from that solely driven by the concentration gradient. The double-diffusive convection in a porous medium, i.e. the convection flow driven by a destabilizing temperature gradient and a stabilizing concentration gradient, has been extensively studied due to its relevance to geophysical applications, such as in Nield (1968) and Rubin & Roth (1979). They summarized criteria for various boundary conditions and different instability mechanisms were found by linear stability analysis. Malashetty, Pal & Kollur (2010) used the modified Darcy equation to study the effect of the couple-stress parameter. However, for the convective dissolution process, both the geothermal gradient and the concentration gradient drive the convection flow. The effects of the geothermal gradient on convective dissolution have been investigated by using stability analysis and 2-D simulations (Javaheri, Abedi & Hassanzadeh 2010; Islam, Sharif & Carlson 2013; Islam, Lashgari & Sephernoori 2014). In studies by Javaheri *et al.* (2010), Islam *et al.* (2013) and Islam *et al.* (2014), the introduction of the geothermal gradient has little influence on the onset of instability and overall dissolution process. The effects of permeability heterogeneity and reservoir aspect ratio were also included. The convective dissolution with a geothermal gradient in an inclined domain has recently been studied by Guerrero, Prol-Ledesma & Karimi (2020). It was found that the convective dissolution process is less affected by the inclination angle compared with the Rayleigh number and buoyancy ratios.

The present study investigates the convective dissolution with the presence of the geothermal gradient, and focuses on the effects of the temperature gradient. We will conduct systematic 3-D simulations for a wide range of control parameters, and discuss in detail the flow evolution. The rest of the paper is organized as follows. In § 2 we describe the governing equations and numerical methods, along with the explored parameter space. In § 3 we present the main results for the evolution of the flow structures. In § 4 we analyse

the evolution of the fluxes and put the current findings in the context of CO_2 sequestration and discuss their implications. In § 5 we consider the influence of the initial temperature condition. And the conclusions are given in § 6.

2. Governing equations and numerical details

We consider a cubic reservoir of porous medium saturated with brine. The porous medium is assumed to be homogeneous and isotropic with uniform porosity ϕ and permeability K. The reservoir has a length H in all three directions. The top boundary represents the CO_2-saturated brine and has a constant concentration S_{top} of dissolved CO_2. The dissolved CO_2 cannot be transferred out of reservoir through the bottom boundary and will accumulate inside the domain with time. The top and bottom boundaries have constant temperature T_{top} and T_{bot}, respectively. We set $T_{bot} > T_{top}$ so that a constant unstable temperature difference $\Delta T = T_{bot} - T_{top}$ is maintained across the reservoir. A linear equation of state is employed for density as $\rho = \rho_0(1 - \beta_T T + \beta_S S)$. Here, ρ_0 is the density of a reference state; T and S are the temperature and concentration deviations from the corresponding values at the same reference state; β_T and β_S are the linear coefficients relating the density variation to the temperature and concentration variations. In the present study we choose the reference state with temperature T_{top} and zero concentration.

2.1. *Governing equations*

The dynamics of the velocity field $\boldsymbol{u}$ is governed by Darcy's law and the continuity equation. Strictly speaking, the fluid viscosity is not constant due to the dissolution of CO_2. For instance, at the temperature of 323 K and pressure of 30 MPa the viscosity of an aqueous solution of CO_2 increases from 5.64×10^{-4} to 5.73×10^{-4} Pa s when the CO_2 mole fraction increases from 0.0086 to 0.0168 (McBride-Wright, Maitland & Trusler 2015). Nevertheless, this change in viscosity is relatively small and in the current study we employ a constant viscosity for the whole reservoir. The temperature T and concentration S obey the advection–diffusion equations. We denote the vertical coordinate by z and the two horizontal coordinates by x and y, respectively. Then the full governing equations read

$$\nabla \cdot \boldsymbol{u} = 0, \tag{2.1a}$$

$$\boldsymbol{u} = -\frac{K}{\mu}[\nabla p + (\beta_S S - \beta_T T)\rho_0 g \boldsymbol{e}_z], \tag{2.1b}$$

$$\frac{(\rho c)_m}{(\rho c_p)_f} \frac{\partial T}{\partial t} = -\boldsymbol{u} \cdot \nabla T + \kappa_m \nabla^2 T, \tag{2.1c}$$

$$\phi \frac{\partial S}{\partial t} = -\boldsymbol{u} \cdot \nabla S + \phi \kappa_S \nabla^2 S. \tag{2.1d}$$

Here, p is the pressure, g is the gravitational acceleration, $\boldsymbol{e}_z$ is the vertical unit vector, μ is fluid viscosity, c_p is the specific heat of the fluid at constant pressure, c is the specific heat of the solid, κ_m is the overall thermal diffusivity and κ_S is the molecular diffusivity of the concentration field, respectively. The subscript 'm' stands for the effective properties of the whole porous medium, including both solid and fluid. The boundary conditions at the top and bottom boundaries are

$$u_z = 0, \quad T = T_{bot}, \quad \partial_z S = 0, \quad \text{at } z = 0, \tag{2.2a}$$

$$u_z = 0, \quad T = T_{top}, \quad S = S_{top}, \quad \text{at } z = H. \tag{2.2b}$$

Note that we do not introduce boundary conditions for the tangential components of the velocity at the boundaries since, at the top and bottom boundary, the tangential velocity is balanced by the tangential gradient of pressure. Periodic boundary conditions are applied in the horizontal directions for all quantities.

The above governing equations are non-dimensionalized by using the reservoir height H, the temperature difference ΔT, the concentration at the top boundary S_{top}, the characteristic velocity $U_c = Kg\rho_0\beta_S S_{top}/\mu$ and the characteristic time scale $t_c = \phi H/U_c$, respectively. Then the non-dimensionalized equations are

$$\nabla \cdot \boldsymbol{u} = 0, \tag{2.3a}$$

$$\boldsymbol{u} = -\nabla p + (\Lambda T - S)\boldsymbol{e}_z, \tag{2.3b}$$

$$\sigma \frac{\partial T}{\partial t} = -\boldsymbol{u} \cdot \nabla T + \frac{Le}{Ra_S}\nabla^2 T, \tag{2.3c}$$

$$\frac{\partial S}{\partial t} = -\boldsymbol{u} \cdot \nabla S + \frac{1}{Ra_S}\nabla^2 S. \tag{2.3d}$$

From now on, all the flow quantities are referred to their non-dimensionalized values unless otherwise mentioned. The dimensionless control parameters include the heat capacity ratio σ, the Lewis number Le, the Rayleigh number of concentration field Ra_S and the thermal Rayleigh number Ra_T, which are respectively defined as

$$\sigma = \frac{(\rho c)_m}{\phi(\rho c_p)_f}, \quad Le = \frac{\kappa_m}{\phi\kappa_S}, \quad Ra_S = \frac{KHg\rho_0\beta_S S_{top}}{\kappa_S\mu\phi}, \quad Ra_T = \frac{KHg\rho_0\beta_T\Delta T}{\kappa_m\mu}. \tag{2.4a–d}$$

The density ratio $\Lambda = (\beta_T\Delta T)/(\beta_S S_{top}) = Ra_T Le/Ra_S$ will also be used below to measure the strength of the temperature difference relative to the initial concentration difference. The non-dimensionalized boundary conditions are the top and bottom boundaries are

$$u_z = 0, \quad T = 1, \quad \partial_z S = 0, \quad \text{at } z = 0, \tag{2.5a}$$

$$u_z = 0, \quad T = 0, \quad S = 1, \quad \text{at } z = 1. \tag{2.5b}$$

2.2. *Physical properties of the fluid and reservoirs*

In order to determine the parameter range of the current study, we review the typical reservoir conditions reported in the existing literature. Considering the reservoirs as a porous medium, the permeability is usually in the range of $K = 10^{-15}$–10^{-12} m^2 (Kopp, Class & Helmig 2009; Huppert & Neufeld 2014; Emami-Meybodi 2017) and the porosity in the range of $\phi = 0.05$–0.4 (Bachu & Adams 2003; Van Der Meer 2005; Hassanzadeh, Pooladi-Darvish & Keith 2006; Kopp *et al.* 2009; Emami-Meybodi 2017). The reservoir thickness can vary from $H = 10$ to 300 m (Bachu & Stewart 2002; Bachu & Adams 2003; Ennis-King & Paterson 2003; De Silva, Ranjith & Perera 2015; Emami-Meybodi 2017). Typical values of the viscosity and density of the pore fluid are $\mu = 10^{-4}$–10^{-3} Pa s and $\rho_0 = 945$–1273 kg m^{-3}, respectively (Bachu & Carroll 2005; Huppert & Neufeld 2014). The solubility of CO_2 in the pore fluid depends on the pressure, temperature and salinity of the brine (Bentham & Kirby 2005; Bachu 2015; De Silva *et al.* 2015; Luo *et al.* 2022), and the density increment due to the CO_2 dissolution can be from 0.1 % up to approximately 3 % (Bachu & Adams 2003; Pau *et al.* 2010; Luo *et al.* 2022), which gives a density difference of approximately $\Delta\rho_S = 1$–30 kg m^{-3}. *In situ* measurements indicate
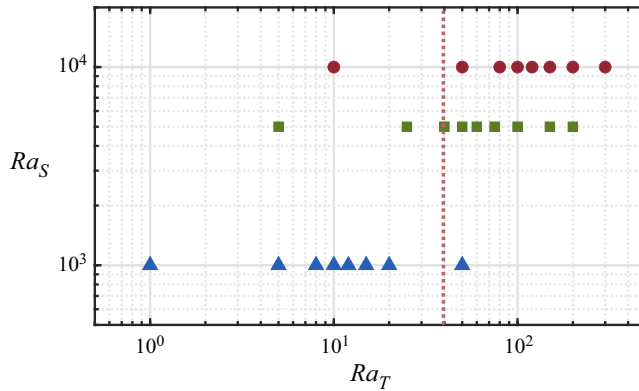
Figure 1. The parameter space explored in the current simulations. For all cases $\sigma = 1$ and $Le = 100$, and for each Ra_S the corresponding case with $Ra_T = 0$ is also simulated. The red vertical dashed line marks the critical value $Ra_T^{cr} = 4\pi^2$ predicted by linear instability analysis for convection driven by a constant temperature difference.

the typical geothermal gradient in the range of $G = 20\text{--}65\,°\text{C}\,\text{km}^{-1}$ (Rao *et al.* 2001; Bachu & Stewart 2002; Nordbotten *et al.* 2005; Kopp *et al.* 2009; Yang *et al.* 2010; De Silva *et al.* 2015). Then, taking a thermal expansion coefficient β_T in the range $3 \times 10^{-4}\text{--}8 \times 10^{-4}\,\text{K}^{-1}$ (Javaheri *et al.* 2010), the density difference induced by the temperature difference can be estimated as $\Delta\rho_T = 0.1\text{--}10\,\text{kg}\,\text{m}^{-3}$. The molecular diffusivity and overall thermal diffusivity are typically of the order of 10^{-9} and $10^{-7}\,\text{m}^2\,\text{s}^{-1}$, respectively (Hassanzadeh *et al.* 2006; Javaheri *et al.* 2010; Emami-Meybodi 2017).

Given the typical values of physical and reservoir properties discussed above, the non-dimensional parameters defined in (2.4*a*–*d*) can be readily estimated. The concentration Rayleigh number Ra_S can reach over 10^5, while for a basin with a large thermal gradient and thickness, the thermal Rayleigh number Ra_T can be as high as 10^3. It should also be pointed out that, for the current flow configuration, the density difference induced by the concentration field is determined by the constant concentration S_{top} which is related to the dissolution process of supercritical CO_2, and that induced by the temperature difference is determined by both the thermal gradient and the reservoir thickness. Therefore, even for a fixed thermal gradient, the density ratio Λ increases as the thickness becomes larger since S_{top} should not depend on thickness. Taking all these and the computing resources into consideration, our simulations explore the parameter range with $10^3 \leq Ra_S \leq 10^4$ and $0.1 \leq \Lambda \leq 5$, with the highest thermal Rayleigh number $Ra_T = 300$. We also fix $\sigma = 1$ and $Le = 100$ for all simulations. The parameter space is shown in figure 1. Note that in the figure we also show the critical value $Ra_T^{cr} = 4\pi^2$ predicted by the linear instability analysis for a convection flow solely driven by a constant temperature difference between the top and bottom boundaries (Horton & Rogers 1945). Therefore, for some cases Ra_T is below Ra_T^{cr} while for the others it is above Ra_T^{cr}.

2.3. *Numerical methods*

The governing equations (2.3) are numerically solved using our in-house code which was originally designed for wall-bounded convection turbulence (Ostilla-Mónico *et al.* 2015). The code employs a second-order finite difference scheme for spatial discretization with staggered grids. For the time advance of the advection–diffusion equations for T and S,

a second-order Runge–Kutta method is used with the nonlinear advection terms treated by a scheme similar to the explicit Adams–Bashforth method and the diffusion terms by a scheme similar to the semi-implicit Crank–Nicolson method. To solve the velocity and pressure fields at each time step, we take the divergence of (2.3*b*) and use the continuity equation (2.3*a*), which gives the following Poisson equation for pressure:

$$\nabla^2 p = \Lambda \partial_z T - \partial_z S, \tag{2.6}$$

with the boundary conditions

$$\partial_z p = \Lambda T - S, \quad \text{at } z = 0, 1. \tag{2.7}$$

Once the pressure field is obtained, the velocity field can be readily computed from (2.3*b*). Moreover, to efficiently solve the concentration field with relatively small diffusivity, the multiple grid strategy is used as in Ostilla-Mónico *et al.* (2015). Specifically, the concentration field is solved on a refined mesh, and the other quantities on a base mesh.

Initially, the velocity is set to zero and the temperature has a vertically linear distribution. The initial concentration field is uniform and equal to a small positive value within the domain to avoid any unphysical negative value during the simulation. A hyperbolic tangent function is applied to introduce a smooth transition between the concentration at the top boundary and the initial value at the interior of the domain. Random perturbations with a magnitude of 10^{-3} are introduced to trigger the convective motions. With these initial conditions, the 3-D simulations are conducted systematically for the parameters stated in figure 1. The details of the numerical settings are summarized in the Appendix. As a validation of our numerical method, we conducted a simulation of RDC at $Ra = 10^4$ with the same flow configuration as Pirozzoli *et al.* (2021). By using the same definition of the Nusselt number, our numerical measurements show $Nu = 98.44$, which is close to 99.84 given by Pirozzoli *et al.* (2021).

3. Flow structures

In the current simulations, initially the concentration field is unstably stratified only at the top boundary, exactly where the convective motions develop first. Moreover, the extra unstable temperature difference may also affect the evolution of the flow. One may anticipate that, for a weak temperature difference, the flow should be very similar to that without a temperature difference. When the temperature difference is large enough to drive the convective motions, it is very likely that the flow evolution is strongly altered.

This is indeed the case, and we demonstrate this by comparing the two simulations with $Ra_T = 10$ and 300 for fixed $Ra_S = 10^4$. The former case has $Ra_T < Ra_T^{cr}$ and the latter has $Ra_T > Ra_T^{cr}$. We first compare the time history of the root-mean-square (r.m.s.) value of the vertical velocity u_z^{rms} for the two cases, see figure 2. Meanwhile, the concentration, temperature and vertical velocity fields on a vertical plane at four different moments are shown in figure 3. During the initial growth of the flow motions, at approximately $t < 2.5$, the increase of u_z^{rms} is very similar between the two cases. At this stage, the flow motions are mainly driven by the large concentration gradient near the top boundary, and the dominant structures are the concentration fingers originated from the top plate, as shown in figure 3(*a*). The fingers extend to similar height for the two cases and both temperature fields are nearly undisturbed. The vertical velocity fields have similar structures to concentration fingers.

As the flow further develops, the influence of the temperature gradient begins to arise, see figure 3(*b–d*). For the case with $Ra_T = 10$, finger structures continue to grow
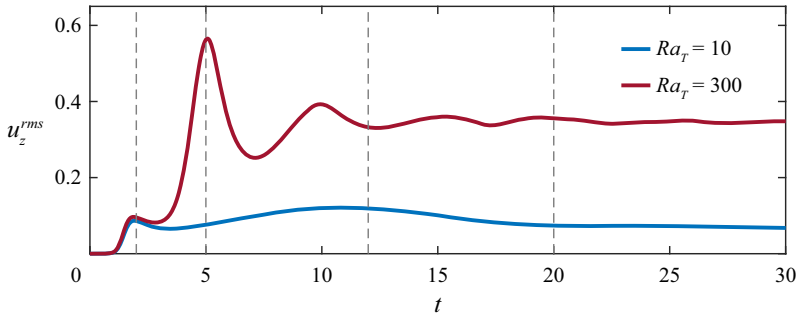
Figure 2. The time history of the r.m.s. of the vertical velocity u_z for two cases with $Ra_T = 10$ and $Ra_T = 300$ and fixed $Ra_S = 10^4$. The four dashed vertical lines mark the time at which the slices are shown in figure 3.
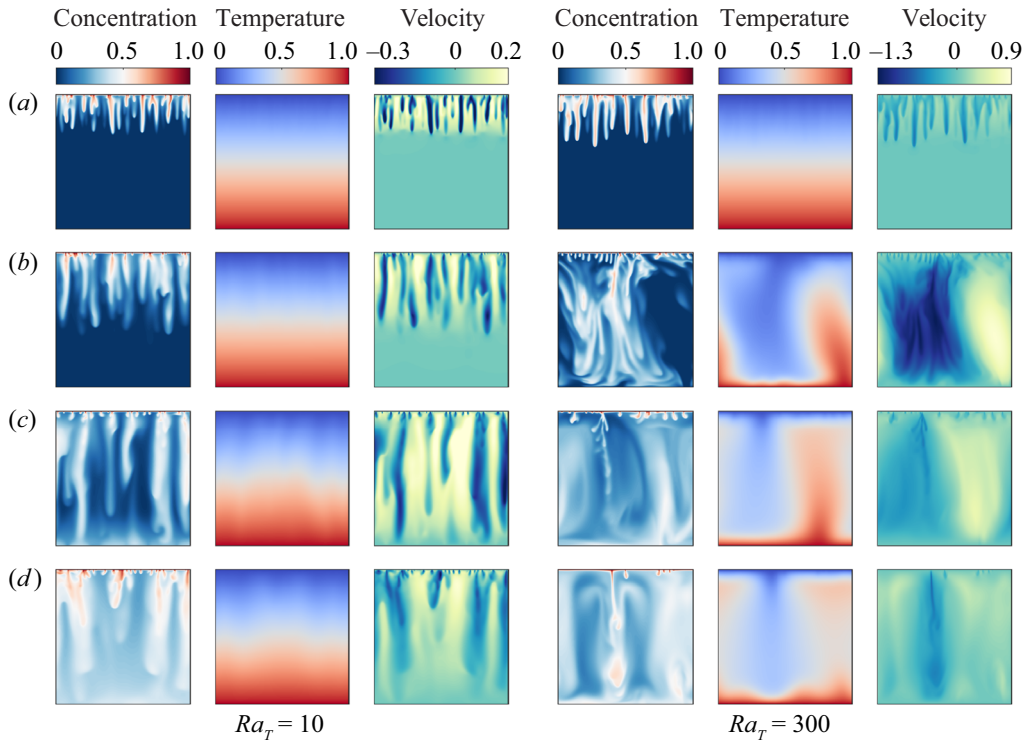

Figure 3. The concentration, temperature and vertical velocity contours on a vertical slice at different moments. Panels (*a–d*) show $t = 2.0$, 5.0, 12.0, and 20.0, respectively. The three columns on the left are for the case with $Ra_T = 10$, and the three columns on the right for the case with $Ra_T = 300$. For both cases $Ra_S = 10^4$.

downward and reach the bottom boundary. The temperature field only exhibits weak oscillations which have a similar characteristic width as the fingers, indicating that they are induced by the fingering motion. The vertical velocity field shows that downwelling fingers move fastest. Fingers randomly distribute in the horizontal direction. Meanwhile, for the case with $Ra_T = 300$, which is considerably larger than $Ra_T^{cr} = 4\pi^2$, the temperature difference drives the large-scale convection rolls which appear later than the fingers driven
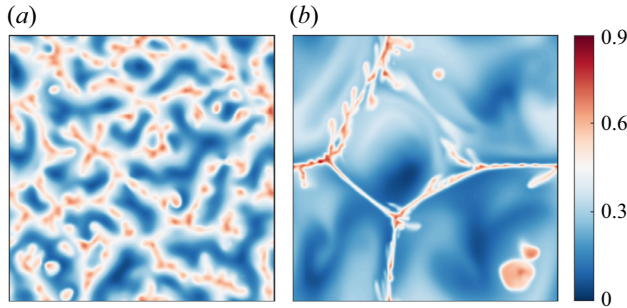
963 A23-8

Figure 4. The concentration contours on the horizontal slice $z = 0.9$ at the time $t = 10$ for the cases with (a) $Ra_T = 10$ and (b) $Ra_T = 300$. For both cases $Ra_S = 10^4$.

by the concentration gradient. The large-scale rolls cause the peak at $t = 5$ in the time history of u_z^{rms} shown in figure 2. The finger structures are also strongly modulated by these large-scale roles: fingers cluster into the descending currents generated by the convection rolls and are suppressed by the upwelling currents. Therefore, inhomogeneity develops in the horizontal distributions of concentration fingers. The large-scale rolls also have larger vertical velocity compared with finger structures, which is in agreement with the larger u_z^{rms} for $Ra_T = 300$ after the initial growth in figure 2.

This inhomogeneity can be clearly seen in the concentration contours on the horizontal slice $z = 0.9$ and at the time $t = 10$, as shown in figure 4. Panel (a) displays the concentration field for the case with $Ra_T = 10$, and all the high concentration patches are the cross-sections of finger structures. Indeed they are distributed randomly on the horizontal plane. While in (b), for the case with $Ra_T = 300$, the high concentration regions follow long and thin filaments, where the downwelling currents of the large-scale rolls are located.

Figure 5 further demonstrates the influence of the temperature difference by comparing the temporal evolution of the horizontally averaged concentration and the temperature profiles for the same two cases. For the case with smaller $Ra_T = 10$, the mean temperature profiles are almost linear during the entire simulation. As the finger structures develop, a high concentration region extends downwards. Interestingly, as the fingers reach the bottom boundary, they directly transport concentration to the bottom region where the mean concentration rises before the bulk region. This phenomenon appears at around $t = 10$ as shown in figure 5(a). As the concentration accumulates at the bottom, the density difference across the domain decreases and the flow motions become weaker, corresponding to the gradually decreasing u_z^{rms} shown in figure 2; see the blue line after $t > 10$.

For the other case with $Ra_T = 300$, the large-scale rolls driven by the temperature field appear at approximately $t = 5$, and figure 5(d) reveals that the temperature field quickly becomes homogeneous afterwards. The large-scale rolls quickly transport the high concentration fluid to the lower part of the domain, and the low concentration fluid to the upper part; see the profiles just after $t = 5$ shown in figure 5(c). These overturns in mean profiles are clearly the footprint of the large-scale convection rolls induced by the temperature difference. The overturn happens several times and then the mean concentration distribution is homogenized in the bulk.
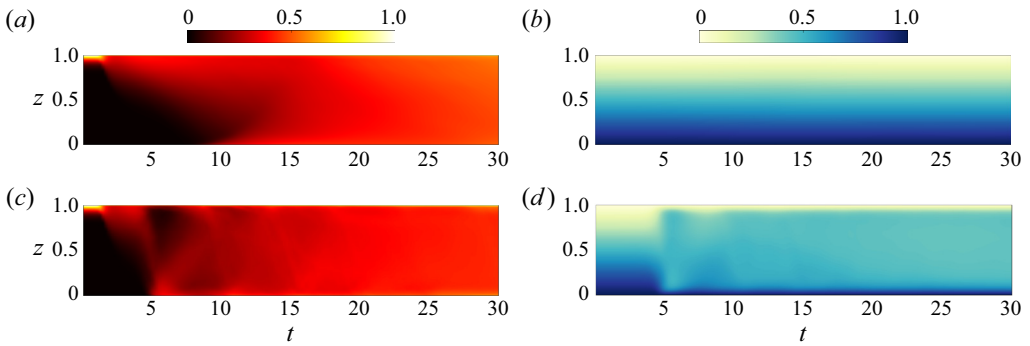
Figure 5. The time evolution of the spatially averaged profiles for the cases with (*a,b*) $Ra_T = 10$ and (*c,d*) $Ra_T = 300$. For both cases $Ra_S = 10^4$. Panels (*a,c*) show the averaged concentration profiles and (*b,d*) the averaged temperature profiles.
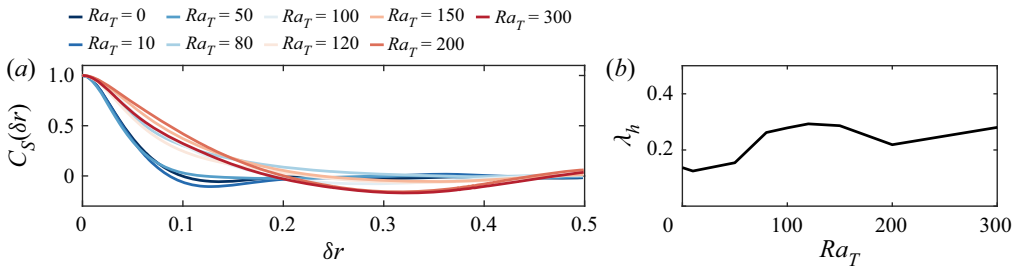

Figure 6. (*a*) The autocorrelation function $C_S(\delta_r)$ and (*b*) the variation of horizontal length scale vs the thermal Rayleigh number for fixed $Ra_S = 10^4$.

To quantitatively reveal the horizontal length of the flow structures, we calculate the autocorrelation function of concentration field as

$$C_S (\delta r) = \frac{\langle [S(r) - \mu_S] [S(r + \delta r) - \mu_S] \rangle_h}{\sigma_S^2}, \tag{3.1}$$

where μ_S and σ_S are the mean and standard deviation of concentration, and $\langle\ \rangle_h$ stands for the average over a horizontal slice during the time period $t = 20$–30; $r = (x, y)$ is the position vector within the horizontal plane; δr is the separation vector with $\delta r = |\delta r|$. The horizontal plane at the height where u_z^{rms} is the largest is used. Then, the typical horizontal length λ_h can be extracted as the separation δr at the first minimum of $C_S(\delta r)$. Figure 6(*a*) displays the 1-D autocorrelation function $C_S(\delta r)$ for all the cases with $Ra_S = 10^4$, and the dependence of λ_h on the thermal Rayleigh number is plotted in figure 6(*b*). It is evident that λ_h first increases with Ra_T as the dominant structures change from fingers to convection rolls, and then does not change much as Ra_T further increases.

4. Transport properties

4.1. *Evolution of Nusselt numbers*

One of the key questions for the current flow is the rate at which the dissolved CO_2 is transferred downwards. Since the bottom boundary is impermeable for the CO_2 concentration, the concentration flux is measured at the top boundary as, by the
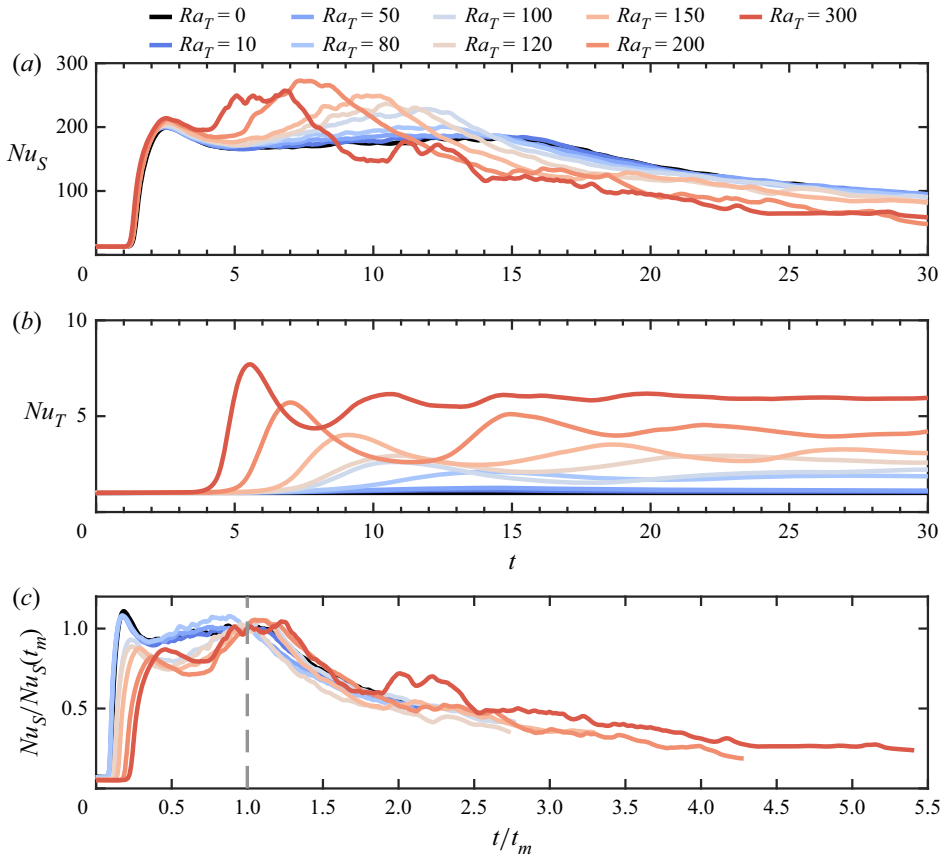
Figure 7. Temporal evolution of (*a*) concentration Nusselt number $Nu_S(t)$, (*b*) temperature Nusselt number $Nu_T(t)$ and (*c*) normalized concentration Nusselt number for $Ra_S = 10^4$. Colours from cold to warm correspond to increasing Ra_T.

non-dimensional quantities,

$$Nu_S(t) = \langle \partial_z S|_{z=1} \rangle_h = \int_0^1 \int_0^1 \partial_z S|_{z=1} \mathrm{d}x \, \mathrm{d}y. \tag{4.1}$$

Meanwhile, the heat flux is calculated as the mean of the fluxes through the top and bottom boundaries as

$$Nu_T(t) = \tfrac{1}{2}(\langle \partial_z T|_{z=1} \rangle_h + \langle \partial_z T|_{z=0} \rangle_h). \tag{4.2}$$

In figure 7 we plot the complete time evolution of $Nu_S(t)$ and $Nu_T(t)$ for fixed $Ra_S = 10^4$ and increasing Ra_T. For the case with $Ra_T = 0$, i.e. without a temperature difference, the time history of $Nu_S(t)$ is very similar to those reported in Hewitt *et al.* (2013). Initially, the concentration flux is dominated by the diffusion process and remains at a small value. When the convective motions start to develop at the top boundary at $t \approx 1$, Nu_S increases exponentially and reaches a maximum at approximately $t = 2.5$. After this peak Nu_S decreases and then maintains a nearly constant value until $t = 15$, and the flow is in an intermediate quasi-steady state. Then, Nu_S continues to slowly decrease until the end of the simulation at $t = 30$. This last stage with decreasing Nu_S is identified as the shutdown process by Hewitt *et al.* (2013).
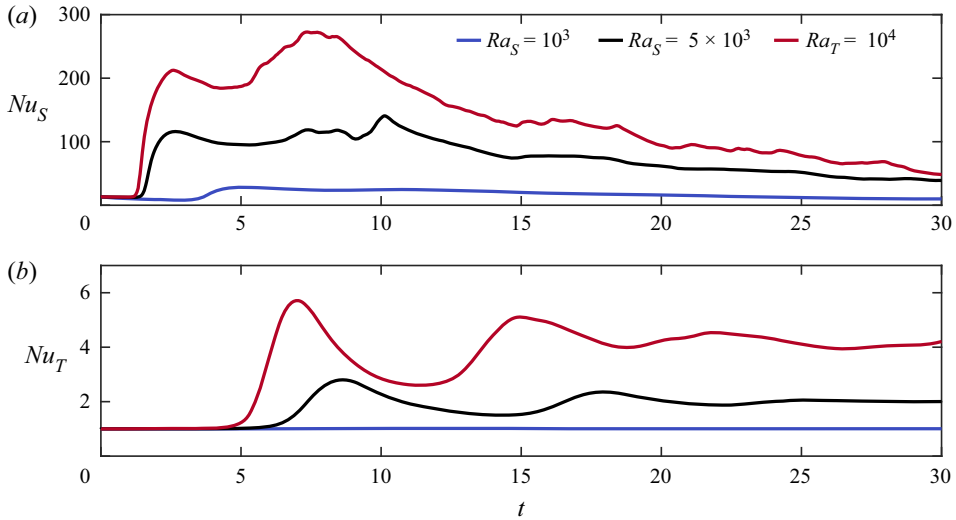
Figure 8. The time evolution of fluxes for three cases with fixed $\Lambda = 2$ and increasing Ra_S.

When the temperature difference is introduced across a layer of porous medium, different evolution behaviours are observed for different Ra_T. For small Ra_T, the time history of Nu_S does not change much compared with the case without a temperature difference, which is expected. The value of Nu_T increases slightly from unity when the convective motions induced by the concentration field become apparent. For large Ra_T, the temperature difference alone is strong enough to drive convective motions, and Nu_T can be higher than unity after a certain time. The value of Nu_T first quickly increases and then oscillates around a final value. The initial increase of Nu_T happens earlier and the final value becomes larger for higher Ra_T. This second scenario occurs when Ra_T is considerably larger than the critical value Ra_T^{cr}, which we refer to as the high Ra_T cases.

The comparison between the time history of Nu_S and that of Nu_T reveals that, for the high Ra_T cases, Nu_S starts to increase at an earlier time than Nu_T does. Together with the flow evolution shown in the previous section, one discovers that the initial increase of Nu_S corresponds to the finger structures driven by the concentration gradient near the top boundary, while the initial increase of Nu_T happens roughly at the same time as when the large-scale rolls driven by the temperature difference emerge. The appearance of these large-scale rolls also destroys the quasi-steady state which exists in the low Ra_T cases and the flow directly enters the final shutdown process, which will be further discussed in § 4.2.

The above discussions suggest that the large-scale rolls driven by the temperature difference have two opposite effects on the concentration transport. At the early stage, the appearance of large-scale rolls greatly enhances the downward transport rate of the concentration field. At the later stage, however, the non-dimensional concentration flux is suppressed for the cases with high Ra_T. This latter effect is due to the fact that the upwelling currents of the large-scale rolls can prevent the descent of high concentration fingers near the top boundary, which can be observed in figure 3(c,d). Moreover, the larger concentration flux carried by the downwelling currents of large-scale rolls accelerates the accumulation of high concentration at the bottom region and the transition towards the shutdown process.

During the final shutdown stage, the time history of Nu_S exhibits self-similarity for different Ra_T. To demonstrate this, we normalize the time t by t_m when Nu_T reaches the

963 A23-12

first maximum, and Nu_S by the value $Nu_S(t_m)$. The rescaled plot is shown in figure 7(*c*). One observes that all the curves for different Ra_T collapse to certain extent for the range $t/t_m > 1$. This enables us to develop a theoretical model for the shutdown stage as described in the following subsection.

As a final remark on the evolution of the fluxes, we plot the time history of Nu_S and Nu_T for three cases with fixed $\Lambda = 2$ and increasing Ra_S in figure 8. The thermal Rayleigh number Ra_T then increases accordingly. For the smallest $Ra_S = 10^3$, $Ra_T = Ra_S \Lambda / Le = 20$ which is below Ra_T^{cr} and the temperature gradient shows a very minor effect on the fluxes. As Ra_T becomes higher than Ra_T^{cr} for the two cases with $Ra_S = 5 \times 10^3$ and 10^4, similar behaviours are observed as those shown in figure 7 with large Ra_T. For larger Ra_T, the large-scale convection rolls develop within a shorter time period and Nu_T starts to rise earlier, which causes the faster transition of the flow into the final shutdown stage.

4.2. *A theoretical model for the shutdown stage*

Following the procedure in Hewitt *et al.* (2013), we present a theoretical model to describe the temporal variations of concentration flux and volume averaged concentration during the final shutdown stage. We define the instantaneous volume averaged concentration as

$$\mathcal{S}(t) = \int_0^1 \int_0^1 \int_0^1 S(x, y, z, t) \, \mathrm{d}x \, \mathrm{d}y \, \mathrm{d}z. \tag{4.3}$$

At any given time *t*, if we integrate the concentration equation (2.3*d*) over the entire domain, then by using the boundary conditions and the definition of $Nu_S(t)$ it is easy to obtain

$$\frac{\mathrm{d}\mathcal{S}}{\mathrm{d}t} = \frac{1}{Ra_S} Nu_S(t). \tag{4.4}$$

The above ordinary differential equation can be closed by an appropriate relation between $Nu_S(t)$ and $\mathcal{S}(t)$. Similar to Hewitt *et al.* (2013), we use the relation between the Nusselt number and the Rayleigh number for the convection in a porous medium driven by a constant concentration difference across the layer. Since the current flow is constantly evolving, the instantaneous Nusselt and Rayleigh numbers must be defined properly. At any given time, the actual concentration difference, which provides part of the driving force, can be approximated as $1 - \mathcal{S}(t)$, while the constant temperature difference also contributes to the driving force of the system. Then an effective total Rayleigh number, which measures the strength of the actual driving force, can be defined as

$$Ra_e(t) = Ra_S[1 - \mathcal{S}(t)] + Ra_T. \tag{4.5}$$

The effective Nusselt number at any time, which should be rescaled by the actual concentration difference, can be calculated as

$$Nu_e(t) = \frac{Nu_S(t)}{1 - \mathcal{S}(t)}. \tag{4.6}$$

Then, as suggested by Hewitt *et al.* (2013) and Hewitt *et al.* (2014), a linear scaling can be applied to the relation between the effective Nusselt number and the effective Rayleigh number as

$$Nu_e(t) = 4\alpha Ra_e(t), \tag{4.7}$$

where α is a scaling coefficient and will be discussed later.

With the help of (4.6), (4.5) and (4.7), equation (4.4) can be closed and gives

$$\frac{\mathrm{d}\mathcal{S}}{\mathrm{d}t} = \frac{1-\mathcal{S}}{Ra_S} 4\alpha \left[Ra_S(1-\mathcal{S}) + Ra_T\right]. \tag{4.8}$$

The solution of the above equations can be readily obtained. For the case without a thermal gradient, for $Ra_T = 0$, the solution reads

$$\mathcal{S}(t) = 1 - (C_0 + 4\alpha t)^{-1}, \tag{4.9}$$

which is the same as that given in Hewitt *et al.* (2013). Here, C_0 is some integral constant and will be determined from the simulation results. The corresponding Nusselt number is

$$Nu_S(t) = 4\alpha Ra_S \left(C_0 + 4\alpha t\right)^{-2}. \tag{4.10}$$

When $Ra_T > 0$, the solution takes a more complex form as

$$\mathcal{S}(t) = 1 - \frac{Ra_T}{Ra_S} \left[C_0 \exp\left(\frac{4\alpha Ra_T t}{Ra_S}\right) - 1\right]^{-1}. \tag{4.11}$$

And the Nusselt number is

$$Nu_S(t) = 4\alpha \frac{Ra_T^2}{Ra_S} \left[C_0 \exp\left(\frac{4\alpha Ra_T t}{Ra_S}\right) - 1\right]^{-1} \left[\left(C_0 \exp\left(\frac{4\alpha Ra_T t}{Ra_S}\right) - 1\right)^{-1} + 1\right]. \tag{4.12}$$

The above solutions contain two parameters, namely α and C_0, which need to be determined from the numerical results.

We first look at the coefficient α. Note that the linear scaling (4.7) is adopted from the RDC driven by a constant temperature difference. Here, the value of α will also be affected by the strength of thermal difference. In order to determine the value of α, one notices that, by using the expressions for $\mathcal{S}(t)$ and $Nu_S(t)$,

$$\alpha = \frac{Nu_S}{4(1-\mathcal{S})\left[Ra_S(1-\mathcal{S}) + Ra_T\right]}. \tag{4.13}$$

The time variations of α for all the cases with $Ra_S = 10^4$ are shown in figure 9. For all cases α is almost constant during the last ten time units, especially for the cases with small Ra_T. We therefore calculate the mean $\bar{\alpha}$ over the time period $20 \leq t \leq 30$. Then the value of C_0 is then determined by fitting the curve of $\mathcal{S}(t)$ over the same time period. The values of $\bar{\alpha}$ and C_0 are summarized in table 1. In figure 10 we compare the theoretical model with the numerical results for all the cases with $Ra_S = 10^4$. The agreement between the model and the numerical curves is very good, especially during the final time period. Numerical results also indicate that a similar agreement is achieved for the cases with $Ra_S = 10^3$ and 5×10^3.

The variation of $\bar{\alpha}$ vs Ra_T is plotted in figure 11 for all cases. At small Ra_T, $\bar{\alpha}$ is nearly independent of Ra_T but decreases as Ra_S increases. For the two higher Ra_S considered here, $\bar{\alpha}$ is very close to those reported in Hewitt *et al.* (2014). When Ra_T is large enough, $\bar{\alpha}$ exhibits a consistent dependence on Ra_T for all the cases with different Ra_S, gradually decreasing with Ra_T. For the highest $Ra_T = 300$, $\bar{\alpha}$ is below 0.005. One possible explanation for the decrease of $\bar{\alpha}$ can be attributed to the difference between the flow morphology at small Ra_T and that at large Ra_T. As shown in figures 3 and 4,
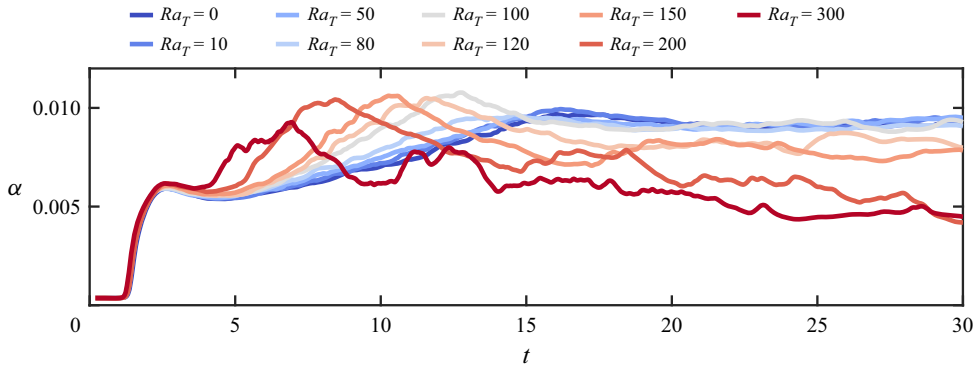
963 A23-14

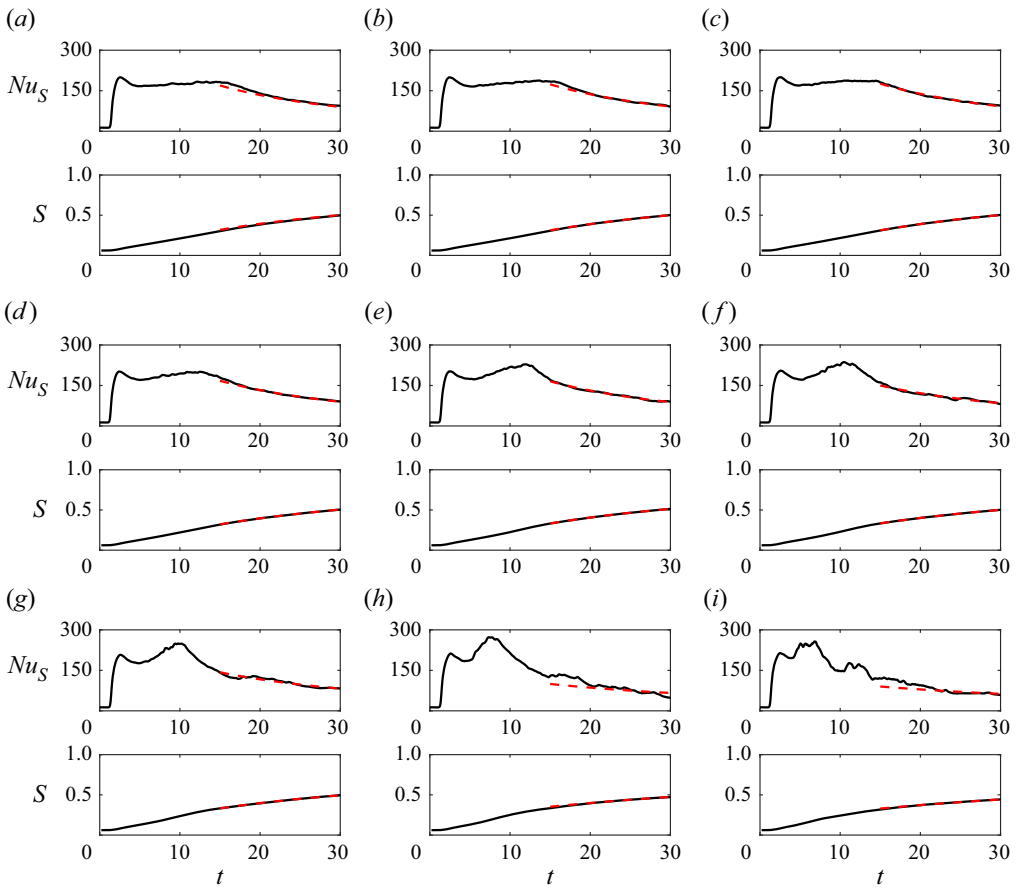Figure 9. Time evolution of α for all the cases with $Ra_S = 10^4$.

Figure 10. Solid lines show the variations of concentration Nusselt number $Nu_S(t)$ and the volume averaged concentration $\mathcal{S}(t)$ vs time, while the dashed lines are the predictions of model (4.9) and (4.11). Panels (*a–i*) show $Ra_T = 0, 10, 50, 80, 100, 120, 150, 200$ and 300, respectively; $Ra_S = 10^4$ for all cases.
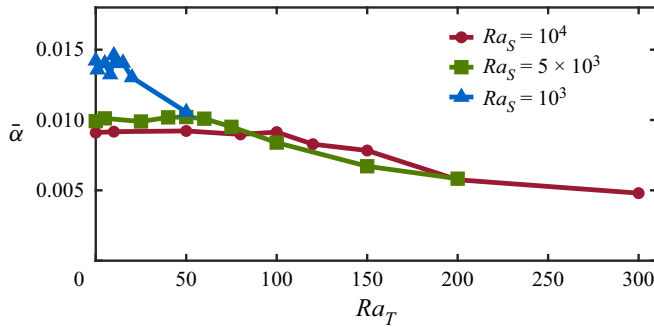
Figure 11. The coefficient $\bar{\alpha}$ vs the thermal Rayleigh number Ra_T for all cases.

at small Ra_T the concentration fingers develop over the whole domain and the flow is fully three-dimensional. While at large Ra_T, fingers mainly develop in the region the downwelling currents induced by the large-scale convection rolls driven by the thermal gradient. That is, the flow morphology is more similar to the quasi-2-D flow over the narrow sheet-like region of downwelling currents. Previous studies suggest that the scaling coefficient α takes different values for 2-D and 3-D flows. For 3-D flows, Hewitt *et al.* (2014) suggests $\alpha \approx 0.0096$, while for 2-D flows α is smaller and around 0.0069 (Hewitt, Neufeld & Lister 2012). These values are very similar to those at small Ra_T and large Ra_T in the current flow.

4.3. *Dissolved carbon dioxide*

In the previous section we discussed the evolution of flow structures and fluxes. In this subsection we focus on the total carbon dioxide which is transported during the entire simulation time. The total CO_2 transferred through the top boundary into the domain at given time t can be calculated by the following integration:

$$M_S(t) = \int_0^t Nu_S(\tau) \, d\tau. \tag{4.14}$$

Figure 12(*a*) shows $M_S(t)$ for all cases with $Ra_S = 10^4$; $M_S(t)$ exhibits non-monotonic variations as Ra_T increases. Let $M_S^0(t)$ denote the case with $Ra_T = 0$, then for small Ra_T, namely $Ra_T \leq 100$ in the current study, $M_S(t)$ is larger than $M_S^0(t)$ during the entire simulation time $0 < t < 30$. When Ra_T is high enough, first $M_S(t)$ is larger than $M_S^0(t)$ and then smaller than $M_S^0(t)$ at the final stage. These variations with increasing Ra_T can be seen more clearly in figure 12(*b*) where the same functions are normalized by $M_S^0(t)$. The transition from $M_S > M_S^0$ to $M_S < M_S^0$ occurs at later time as Ra_T becomes smaller. Due to the limitation of the current simulation time, we do not observe this transition for $Ra_T \leq 100$. For larger Ra_T, there exist two peaks in the time history of M_S/M_S^0. Comparisons with the time history of the two Nusselt numbers shown in figure 7 reveal that the first peak of M_S/M_S^0 for different Ra_T occurs at almost the same time of around $t = 2.5$, which corresponds to the end of the exponential growth of Nu_S. During this initial period, the temperature field does not have significant effects on the fluxes, and the flow is mainly driven by the concentration field. The amplitudes of first peaks vary for different Ra_T because of different initial perturbations before the rapid increase of Nu_S. The second
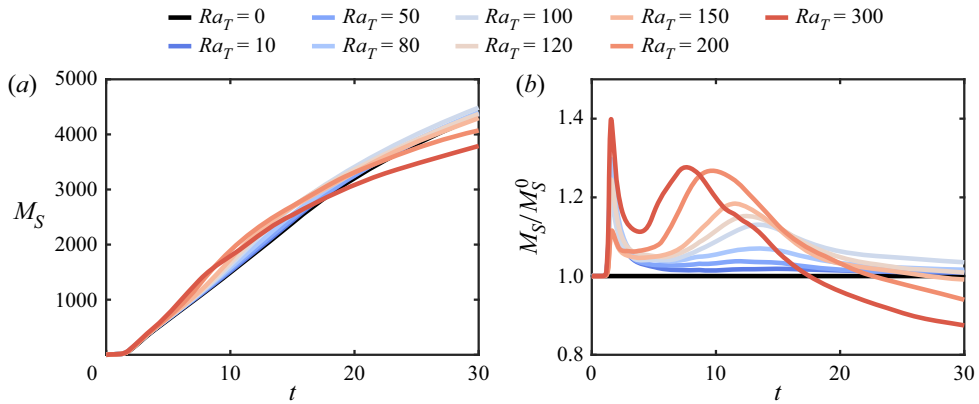
963 A23-16

Figure 12. (*a*) The accumulative transfer of CO_2 as the function of time for the cases with $Ra_S = 10^4$. (*b*) The same functions normalized by that of the case with $Ra_T = 0$. Here, Ra_T increases as the line colour changes from blue to red.
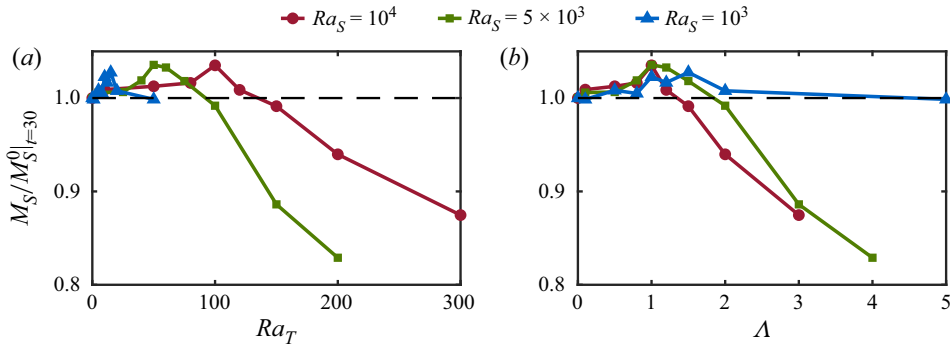

Figure 13. The ratio M_S/M_S^0 at $t = 30$, i.e. the end of the simulation, vs (*a*) the thermal Rayleigh number Ra_T and (*b*) the density ratio Λ.

peak is noticeable for cases with $Ra_T \geq 100$ in figures 7(*a*) and 12(*b*). For each Ra_T the second peak of M_S/M_S^0 is related to the second rise of Nu_S. At this stage, Nu_T is evidently larger than unity at higher Ra_T. The presence of large-scale rolls changes the instantaneous concentration flux at the top boundary, and therefore the total transferred CO_2. It takes less time for the flow to form these rolls at larger Ra_T, which corresponds to an earlier occurrence of the second peak of M_S/M_S^0.

We then look at the total CO_2 transported into the domain at the end of the simulations. Figure 13 displays the ratio M_S/M_S^0 at $t = 30$ vs Ra_T and Λ for all simulated cases. For all three concentration Rayleigh numbers, the ratio first increases then decreases with Λ, see figure 13(*b*). For the smallest $Ra_S = 10^3$, the largest thermal Rayleigh number $Ra_T = 50$ is only slightly higher than the critical value Ra_T^{cr} and the convective motions driven by the thermal gradient are not strong. Still, the additional temperature difference across the domain has noticeable effects on the accumulative transfer of CO_2. As Ra_S increases, the ratio M_S/M_S^0 at $t = 30$ reaches the peak value at larger Ra_T. Moreover, when Ra_T is large enough, the ratio drops below unity, indicating that the total CO_2 transported downwards at $t = 30$ is less than that without the presence of a temperature difference.
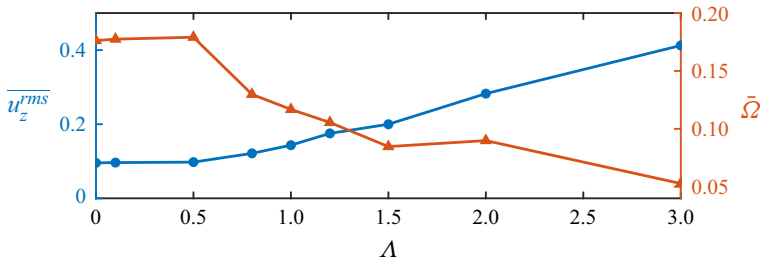
963 A23-17

Figure 14. The averaged $\overline{u_z^{rms}}$ and $\bar{\Omega}$ over the time period $20 \leq t \leq 30$. For all cases $Ra_S = 10^4$.

For the case with $Ra_S = 5 \times 10^3$ and $Ra_T = 200$, the total amount of CO_2 transferred into the domain at $t = 30$ can be reduced by over 17 % compared with the case with $Ra_T = 0$. Interestingly, if the ratio M_S/M_S^0 at $t = 30$ is plotted against the density ratio Λ, see figure 13(*b*), one observes that the ratio reaches the maximum at around $\Lambda = 1$ for all three Ra_S. The maximal increment in M_S induced by the temperature difference is over 3 % for the two larger Ra_S. This non-monotonic trend can be understood as follows. Two opposite effects are introduced by the unstable temperature gradient. On one hand, the vertical flow motions are stronger due to the extra buoyancy force of the thermal field. On the other hand, the concentration fingers are clustered by the large-scale rolls driven by the thermal field. The former will enhance the downward transport while the latter will suppress the transport because of the reduction of the horizontal area with larger concentration.

To quantitatively demonstrate these two effects, we employ the r.m.s. value u_z^{rms} of the vertical velocity and the total area Ω of the regions where $S' > S_{std}$ and $u_z' < -u_z^{std}$. Here, S' and u_z' are the deviations from the horizontally averaged concentration and vertical velocity, while S_{std} and u_z^{std} are the corresponding standard deviations. The two values u_z^{rms} and Ω are calculated over the horizontal plane at the height with maximal u_z^{rms} and then averaged over the time period $20 \leq t \leq 30$. In figure 14 we plot the dependence of $\overline{u_z^{rms}}$ and $\bar{\Omega}$ on the density ratio Λ for fixed $Ra_S = 10^4$. Clearly, $\overline{u_z^{rms}}$ increases with Λ, while $\bar{\Omega}$ decreases. The two curves intersect with each other at some moderate density ratio slightly above unity. Therefore, the maximal M_S/M_S^0 at moderate density ratio is very likely caused by these two competing effects of the thermal field.

For the current flow configuration, the whole domain will eventually have $\mathcal{S} = 1$ when the time approaches infinity. The theoretical model constructed in the previous section can provide some indications about the long-term behaviours of the total dissolved carbon dioxide. By using (4.9) and (4.11) and the coefficients determined from the numerical results, we estimate the time t_{90} when $\mathcal{S} = 0.9$, i.e. where the volume averaged concentration equals to 90 % of the concentration at the top boundary. The values of t_{90} are listed in table 1, and their dependence on Λ is plotted in figure 15. Note that t_{90} is in the non-dimensional form. Figure 15 suggests that overall t_{90} increases with Ra_S. For fixed Ra_S, however, t_{90} generally first decreases and then increases with Λ or equivalently Ra_T. It reaches the minimum around $\Lambda = 1$ for all three Ra_S considered here.

4.4. *Implications for CO$_2$ sequestration*

Above findings reveal that, for high Ra_S, which is very likely the case in a real geological reservoir, a weak to moderate geothermal gradient may increase the total carbon dioxide transferred into the saline aquifer due to convective dissolution during a certain time period, while a strong geothermal gradient may have the
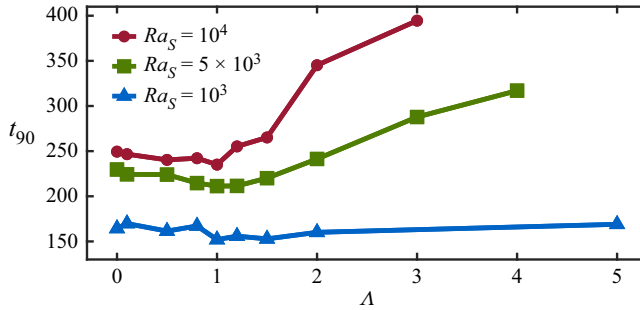
963 A23-18

Figure 15. The time t_{90} when the volume averaged concentration $\mathcal{S}$ reaches 90 % of the top value, as predicted by the theoretical models (4.9) and (4.11).

opposite effect. To demonstrate this in the context of a realistic situation, we take a typical geological reservoir with porosity $\phi = 0.2$, permeability $K = 1.25 \times 10^{-13}\,\mathrm{m}^2$, viscosity $\mu = 2 \times 10^{-4}\,\mathrm{Pa\,s}$, overall thermal diffusivity $\kappa_m = 10^{-7}\,\mathrm{m}^2\,\mathrm{s}^{-1}$ and concentration diffusivity $\kappa_S = 5 \times 10^{-9}\,\mathrm{m}^2\,\mathrm{s}^{-1}$. For brine saturated with CO_2, the density increment is approximately $8\,\mathrm{kg\,m}^{-3}$. Then a 200 m aquifer will give a concentration Rayleigh number $Ra_S = 10^4$ if roughly taking $g = 10\,\mathrm{m\,s}^{-2}$, and the non-dimensional simulation time $t = 30$ corresponds to approximately 760 years. Assuming a geothermal gradient of $50\,^\circ\mathrm{C\,km}^{-1}$, the temperature difference and thermal Rayleigh number across the aquifer are $\Delta T = 10\,^\circ\mathrm{C}$ and $Ra_T = 100$ by using $\beta_T = 8 \times 10^{-4}\,\mathrm{K}^{-1}$, respectively. Therefore, under this circumstance, the density ratio is 1.0. For an aquifer with an area of $100\,\mathrm{km}^2$, approximately 2.4×10^6 tons of extra CO_2 will be transferred into the aquifer from the perspective of convective dissolution with a geothermal gradient during the time period of 760 years.

Furthermore, our results suggest that the large-scale convection rolls driven by the thermal gradient can strongly alter the horizontal pattern of the finger structures. In actual environments, finger structures mainly happen at the interface region between the supercritical CO_2 layer and the brine layer below. However, the large-scale convection rolls may already exist over a layer with much larger thickness and therefore much higher thermal Rayleigh number. Then, the upwelling and downwelling currents of the large-scale rolls can still affect the horizontal distribution of the finger structures, even though the local thermal Rayleigh number across the interface region is much lower. Also, the geothermal gradient may play a non-negligible role in many CO_2-sequestration sites.

5. Influence of initial conditions

In all the cases discussed above, initially, the temperature has a linear distribution between the top and bottom boundaries and the fluid is at rest. For the cases with a strong temperature difference, large-scale rolls usually appear after the finger structures, and the influences of these structures driven by temperature difference do not show up at the beginning. As an idealized model, such initial conditions are easy to implement. In real underground environments with strong enough geothermal gradients, however, large-scale convective motions should already exist when the supercritical CO_2 is injected. Therefore, in this section we investigate the influences of different initial conditions. We take the case with $Ra_S = 10^4$ and $Ra_T = 100$ as the reference case, and refer to the initially linear temperature distribution and zero velocity as case IC1. In order to
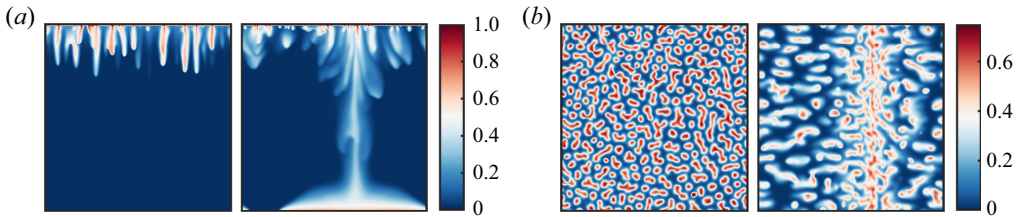
Figure 16. Flow fields at $t = 2$ for two cases with different initial temperature fields. For both cases $Ra_S = 10^4$ and $Ra_T = 100$. (*a*) The concentration contours on a vertical slice. (*b*) The concentration contours on the horizontal slice at $z = 0.9$. Within each panel the left image is for the case starting with a linearly distributed temperature field, and the right image is that with a fully developed thermally driven convection field.

mimic the real environment, we rerun the reference case with the following procedure and refer to this new simulation as case IC2. First, a pure thermally driven convection flow is simulated with $Ra_T = 100$ until the flow fully develops and the large-scale rolls are present. We take an instantaneous velocity field and corresponding temperature field as the initial conditions, and set the concentration at the top plate as S_{top} with $Ra_S = 10^4$. The simulation is then run for another 30 non-dimensional time units.

Figure 16 compares the flow fields of cases IC1 and IC2 at the time $t = 2$. At this time the large-scale rolls in case IC1 have not developed yet. Therefore, flow motions are dominated by finger structures, as shown in the left panel of figure 16(*a*). However, in case IC2, since the large-scale rolls exist at the beginning, at time $t = 2$, high concentration fluid has already been transported to the bottom of domain by the descending currents of the large-scale rolls, see the right panel of figure 16(*a*). The concentration fields on the horizontal plane at $z = 0.9$ also clearly indicate the difference in the horizontal distributions of fingers, as shown in figure 16(*b*). Fingers are randomly distributed in case IC1 but concentrate at the locations of the downwelling current in case IC2. Note that the downwelling currents form a single sheet which spans the whole width of the domain for the case shown in figure 16(*b*), while the case in figure 4(*b*) has multiple sheets intersecting with each other. This difference can be attributed to the different Ra_T. The large-scale convection rolls consist of a pair of 2-D rolls for $Ra_T = 100$, and several convection cells for $Ra_T = 300$.

The evolution of Nu_S, which is plotted in figure 17, is also different between the two cases. In the figure we also plot the simulation with $Ra_T = 0$ for reference. The intermediate quasi-steady stage in the range $5 < t < 15$ in the case without a temperature difference disappears in case IC1 due to the overlap with the development of large-scale rolls. In case IC2, on the other hand, the large-scale rolls are in their fully developed state at the beginning of the simulation, and a new quasi-steady stage with nearly constant Nu_S exists during the time period $3 < t < 8$. The non-dimensional flux during this stage in case IC2 is higher than the other two cases, and the flow enters the final shutdown process at the earliest time among the three cases. The final shutdown process is similar the Nu_S variation for all cases. It should be pointed out that, although different initial conditions can change the temporal evolution of the fluxes and the dynamics of the flow structures, the final state of the system is only determined by Ra_T since, eventually, the interior fluid will be saturated with carbon dioxide and the convective motions are solely driven by temperature difference.
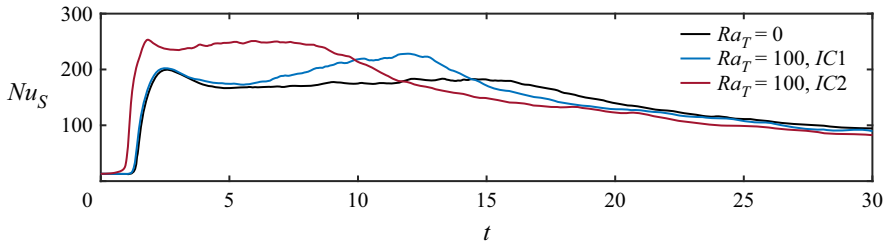
963 A23-20

Figure 17. The temporal evolution of Nu_S for three cases with fixed $Ra_S = 10^4$. The black line shows the case without a temperature difference, the blue line shows the case with a temperature difference and initially linearly distributed temperature field and the red line shows the case with a temperature difference starting from a fully developed thermally driven convection state, respectively.

6. Conclusions

In summary, we study the influence of the unstable thermal gradient on the convective dissolution of CO_2 in 3-D porous media. As a preliminary investigation, we assume all the physical properties are homogeneous and isotropic. Three different concentration Rayleigh numbers are investigated within the range $10^3 \leq Ra_S \leq 10^4$, and for each Ra_S a series of thermal Rayleigh numbers are simulated by using 3-D direct numerical simulation. The explored Ra_T covers the range from below the critical value Ra_T^{cr} to above it. Here, Ra_T^{cr} is the critical value predicted by the linear instability analysis of the porous medium layer experiencing a pure thermal gradient. The simulations are run until 30 non-dimensional time units when the flow is already in the final shutdown process.

When Ra_T is smaller than Ra_T^{cr}, the temperature difference alone cannot drive convection rolls, and the flow is dominated by finger structures driven by the concentration gradient. The development of finger structures is similar to that without a temperature difference. When Ra_T is large enough to trigger the large-scale rolls, the evolution of finger structures is strongly modulated by these large-scale rolls. Fingers grow faster at the regions of downwelling currents of large-scale rolls, and are suppressed by the upwelling currents. Therefore, the horizontal distribution of fingers is no longer uniformly random but is denser at the downwelling regions of large-scale rolls.

The time evolution of fluxes also exhibits different behaviours for different Ra_T. A weak temperature difference only has minor effects on the fluxes. The non-dimensional concentration flux quickly increases when the finger structures develop, then is nearly constant during the intermediate quasi-steady stage and finally decreases as the flow enters the shutdown process. For a strong temperature difference, the large-scale rolls enhance the concentration flux at early times and disrupt the quasi-steady stage. The flow enters the final shutdown process faster as Ra_T becomes larger. The flow evolution is self-similar during the shutdown stage, as indicated by the collapse of rescaled Nu_S for different Ra_T. As Ra_T increases, the concentration structures shift from fingers to large-scale circulations and the dominant width changes accordingly. When the flow is in the shutdown stage, by assuming a well-mixed internal concentration and applying asymptotic linear scaling in RDC to convective dissolution, we obtain the theoretical predictions of the volume averaged concentration and non-dimensional concentration flux, which are consistent with numerical measurements.

The total amount of CO_2 transferred into the domain at the end of simulations shows a non-monotonic dependence on Ra_T for a given Ra_S. It first increases and then decreases with Ra_T. The maximum is reached at approximately unit density ratio, i.e. the density

Ra_S	Ra_T	Λ	$N_x(m_x)$	$N_y(m_y)$	$N_z(m_z)$	$M_S\|_{t=30}$	$\bar{\alpha}$	C_0	t_{90}
10^3	0	0.0	192(2)	192(2)	192(2)	516.32	0.0142	0.6624	164.30
10^3	1	0.1	192(2)	192(2)	192(2)	515.58	0.0136	1.0007	169.77
10^3	5	0.5	192(2)	192(2)	192(2)	520.60	0.0140	1.0035	161.45
10^3	8	0.8	192(2)	192(2)	192(2)	518.86	0.0132	1.0062	167.11
10^3	10	1.0	192(2)	192(2)	192(2)	528.05	0.0146	1.0066	152.01
10^3	12	1.2	192(2)	192(2)	192(2)	524.89	0.0140	1.0084	155.83
10^3	15	1.5	192(2)	192(2)	192(2)	530.52	0.0141	1.0109	152.83
10^3	20	2.0	192(2)	192(2)	192(2)	520.32	0.0130	1.0156	160.09
10^3	50	5.0	192(2)	192(2)	192(2)	515.61	0.0106	1.0498	168.97
5×10^3	0	0.0	288(2)	288(2)	192(2)	2283.30	0.0099	0.8875	229.66
5×10^3	5	0.1	288(2)	288(2)	192(2)	2296.77	0.0101	1.0009	224.35
5×10^3	25	0.5	288(2)	288(2)	192(2)	2298.05	0.0099	1.0045	224.03
5×10^3	40	0.8	288(2)	288(2)	192(2)	2326.51	0.0102	1.0070	214.65
5×10^3	50	1.0	288(2)	288(2)	192(2)	2364.45	0.0102	1.0090	211.32
5×10^3	60	1.2	288(2)	288(2)	192(2)	2358.03	0.0101	1.0109	211.46
5×10^3	75	1.5	288(2)	288(2)	192(2)	2324.87	0.0095	1.0142	220.13
5×10^3	100	2.0	288(2)	288(2)	288(2)	2264.61	0.0084	1.0205	241.34
5×10^3	150	3.0	288(2)	288(2)	288(2)	2023.33	0.0067	1.0310	287.80
5×10^3	200	4.0	384(2)	384(2)	288(2)	1892.80	0.0058	1.0417	317.00
10^4	0	0.0	288(2)	288(2)	288(2)	4333.02	0.0091	0.9202	249.43
10^4	10	0.1	288(2)	288(2)	288(2)	4372.07	0.0092	1.0009	246.65
10^4	50	0.5	288(2)	288(2)	288(2)	4387.61	0.0092	1.0045	240.32
10^4	80	0.8	288(2)	288(2)	288(2)	4403.18	0.0090	1.0074	242.15
10^4	100	1.0	384(2)	384(2)	288(2)	4484.85	0.0091	1.0094	235.07
10^4	120	1.2	384(2)	384(2)	288(2)	4370.94	0.0083	1.0119	255.23
10^4	150	1.5	384(2)	384(2)	288(2)	4295.24	0.0078	1.0153	265.17
10^4	200	2.0	576(2)	576(2)	384(2)	4071.88	0.0058	1.0238	345.17
10^4	300	3.0	576(2)	576(2)	384(2)	3789.90	0.0048	1.0358	394.51

Table 1. Summary of simulations. Columns from left to right are the concentration Rayleigh number, thermal Rayleigh number, density ratio, resolutions in the x-axis, y-axis, z-axis (with refinement factors for multiple resolutions), total CO_2 transferred to the domain at the end time of the simulations, averaged values of α from $t = 20$ to 30, fitted integral coefficient, predicted time to reach $\mathcal{S} = 0.9$.

difference induced by the temperature difference equals that induced by the concentration difference. The implications of the current findings for real CO_2-sequestration are then discussed for typical saline aquifer properties, and suggest that the influence of the geothermal gradient may not be negligible.

To mimic the real environment where large-scale rolls exist long before CO_2 sequestration, we rerun a reference case to examine the influence of initial conditions. Compared with the linear distribution for the initial temperature field, using the fully developed temperature field at the start of simulation can produce a higher quasi-steady stage similar to the case without a thermal gradient. After that the flow also enters the shutdown stage but the flux decays at an earlier time.

Note that the model flow investigated here is different from the double-diffusive convection in porous media, where the temperature and concentration gradients usually have opposite effects on fluid density. The current study opens new directions for the convective dissolution in CO_2-sequestration, and more works are needed for future study.

963 A23-22

Author ORCIDs.

Chenglong Hu https://orcid.org/0000-0002-2935-9258;

Ke Xu https://orcid.org/0000-0002-6791-6393;

Yantao Yang https://orcid.org/0000-0001-5065-2769.

Appendix. Summary of numerical details

The details of the simulations are summarized in table 1. Recall that, for all simulations, the heat capacity ratio and the Lewis number are fixed at $\sigma = 1$ and $Le = 100$, respectively.

REFERENCES

BACHU, S. 2003 Screening and ranking of sedimentary basins for sequestration of CO_2 in geological media in response to climate change. *Environ. Geol.* **44** (3), 277–289.

BACHU, S. 2015 Review of CO_2 storage efficiency in deep saline aquifers. *Intl J. Greenh. Gas Control* **40**, 188–202.

BACHU, S. & ADAMS, J.J. 2003 Sequestration of CO_2 in geological media in response to climate change: capacity of deep saline aquifers to sequester CO_2 in solution. *Energy Convers. Manage.* **44** (20), 3151–3175.

BACHU, S. & CARROLL, J.J. 2005 In-situ phase and thermodynamic properties of resident brine and acid gases (CO_2 and H_2S) injected into geological formations in western Canada. In *Greenhouse Gas Control Technologies 7* (ed. E.S. Rubin, D.W. Keith, C.F. Gilboy, M. Wilson, T. Morris, J. Gale, K. Thambimuthu), pp. 449–457. Elsevier Science.

BACHU, S. & STEWART, S. 2002 Geological sequestration of anthropogenic carbon dioxide in the Western Canada Sedimentary Basin: suitability analysis. *J. Can. Petrol. Technol.* **41** (2), 32–40.

BENTHAM, M. & KIRBY, M. 2005 CO_2 storage in saline aquifers. *Oil Gas Sci. Technol.* **60** (3), 559–567.

CHAN KIM, M. & KYUN CHOI, C. 2012 Linear stability analysis on the onset of buoyancy-driven convection in liquid-saturated porous medium. *Phys. Fluids* **24** (4), 044102.

DE PAOLI, M., ZONTA, F. & SOLDATI, A. 2017 Dissolution in anisotropic porous media: modelling convection regimes from onset to shutdown. *Phys. Fluids* **29** (2), 026601.

DE SILVA, G.P.D., RANJITH, P.G. & PERERA, M.S.A. 2015 Geochemical aspects of CO_2 sequestration in deep saline aquifers: a review. *Fuel* **155**, 128–143.

EMAMI-MEYBODI, H. 2017 Stability analysis of dissolution-driven convection in porous media. *Phys. Fluids* **29** (1), 014102.

EMAMI-MEYBODI, H., HASSANZADEH, H., GREEN, C.P. & ENNIS-KING, J. 2015 Convective dissolution of CO_2 in saline aquifers: progress in modeling and experiments. *Intl J. Greenh. Gas Control* **40**, 238–266.

ENNIS-KING, J. & PATERSON, L. 2003 Role of convective mixing in the long-term storage of carbon dioxide in deep saline formations. In *SPE Annual Technical Conference and Exhibition*, pp. SPE–84344–MS. Society of Petroleum Engineers.

GREEN, C.P. & ENNIS-KING, J. 2018 Steady flux regime during convective mixing in three-dimensional heterogeneous porous media. *Fluids* **3** (3), 58.

GUERRERO, F.J., PROL-LEDESMA, R.M. & KARIMI, N. 2020 Transient thermo-solutal convection in a tilted porous enclosure heated from below and salted from above. *Intl Commun. Heat Mass Transfer* **118**, 104875.

HASSANZADEH, H., POOLADI-DARVISH, M. & KEITH, D.W. 2006 Stability of a fluid in a horizontal saturated porous layer: effect of non-linear concentration profile, initial, and boundary conditions. *Transp. Porous Media* **65** (2), 193–211.

HEWITT, D.R., NEUFELD, J.A. & LISTER, J.R. 2012 Ultimate regime of high Rayleigh number convection in a porous medium. *Phys. Rev. Lett.* **108** (22), 224503.

HEWITT, D.R., NEUFELD, J.A. & LISTER, J.R. 2013 Convective shutdown in a porous medium at high Rayleigh number. *J. Fluid Mech.* **719**, 551–586.

HEWITT, D.R., NEUFELD, J.A. & LISTER, J.R. 2014 High Rayleigh number convection in a three-dimensional porous medium. *J. Fluid Mech.* **748**, 879–895.

HORTON, C.W. & ROGERS, F.T., JR. 1945 Convection currents in a porous medium. *J. Appl. Phys.* **16** (6), 367–370.

HUPPERT, H.E. & NEUFELD, J.A. 2014 The fluid mechanics of carbon dioxide sequestration. *Annu. Rev. Fluid Mech.* **46** (1), 255–272.

ISLAM, A.W., LASHGARI, H.R. & SEPHERNOORI, K. 2014 Double diffusive natural convection of CO_2 in a brine saturated geothermal reservoir: study of non-modal growth of perturbations and heterogeneity effects. *Geothermics* **51**, 325–336.

ISLAM, A.W., SHARIF, M.A.R. & CARLSON, E.S. 2013 Numerical investigation of double diffusive natural convection of CO_2 in a brine saturated geothermal reservoir. *Geothermics* **48**, 101–111.

JAVAHERI, M., ABEDI, J. & HASSANZADEH, H. 2010 Linear stability analysis of double-diffusive convection in porous media, with application to geological storage of CO_2. *Transp. Porous Media* **84** (2), 441–456.

KNEAFSEY, T.J. & PRUESS, K. 2010 Laboratory flow experiments for visualizing carbon dioxide-induced, density-driven brine convection. *Transp. Porous Media* **82** (1), 123–139.

KOPP, A., CLASS, H. & HELMIG, R. 2009 Investigations on CO_2 storage capacity in saline aquifers. *Intl J. Greenh. Gas Control* **3** (3), 263–276.

LUO, A., LI, Y., CHEN, X., ZHU, Z. & PENG, Y. 2022 Review of CO_2 sequestration mechanism in saline aquifers. *Nat. Gas Ind.* B **9** (4), 383–393.

MALASHETTY, M.S., PAL, D. & KOLLUR, P. 2010 Double-diffusive convection in a Darcy porous medium saturated with a couple-stress fluid. *Fluid Dyn. Res.* **42** (3), 035502.

MCBRIDE-WRIGHT, M., MAITLAND, G.C. & TRUSLER, J.P.M. 2015 Viscosity and density of aqueous solutions of carbon dioxide at temperatures from (274 to 449) K and at pressures up to 100 MPa. *J. Chem. Engng Data* **60** (1), 171–180.

MYINT, P.C., BESTEHORN, M. & FIROOZABADI, A. 2012 Effect of permeability anisotropy on buoyancy-driven flow for CO_2 sequestration in saline aquifers. *Water Resour. Res.* **48** (9), W09539.

NEUFELD, J.A., HESSE, M.A., RIAZ, A., HALLWORTH, M.A., TCHELEPI, H.A. & HUPPERT, H.E. 2010 Convective dissolution of carbon dioxide in saline aquifers. *Geophys. Res. Lett.* **37** (22), L22404.

NIELD, D.A. 1968 Onset of thermohaline convection in a porous medium. *Water Resour. Res.* **4** (3), 553–560.

NORDBOTTEN, J.M., CELIA, M.A. & BACHU, S. 2005 Injection and storage of CO_2 in deep saline aquifers: analytical solution for CO_2 plume evolution during injection. *Transp. Porous Media* **58** (3), 339–360.

ORR, F.M., JR. 2009 CO_2 capture and storage: are we ready? *Energy Environ. Sci.* **2** (5), 449–458.

OSTILLA-MÓNICO, R., YANG, Y., VAN DER POEL, E.P., LOHSE, D. & VERZICCO, R. 2015 A multiple-resolution strategy for direct numerical simulation of scalar turbulence. *J. Comput. Phys.* **301**, 308–321.

OTERO, J., DONTCHEVA, L.A., JOHNSTON, H., WORTHING, R.A., KURGANOV, A., PETROVA, G. & DOERING, C.R. 2004 High-Rayleigh-number convection in a fluid-saturated porous layer. *J. Fluid Mech.* **500**, 263–281.

PAU, G.S.H., BELL, J.B., PRUESS, K., ALMGREN, A.S., LIJEWSKI, M.J. & ZHANG, K. 2010 High-resolution simulation and characterization of density-driven flow in CO_2 storage in saline aquifers. *Adv. Water Resour.* **33** (4), 443–455.

PIROZZOLI, S., DE PAOLI, M., ZONTA, F. & SOLDATI, A. 2021 Towards the ultimate regime in Rayleigh–Darcy convection. *J. Fluid Mech.* **911**, R4.

RAO, Y.H., SUBRAHMANYAM, C., SHARMA, S.R., RASTOGI, A.A. & DEKA, B. 2001 Estimates of geothermal gradients and heat flow from BSRs along the Western Continental Margin of India. *Geophys. Res. Lett.* **28** (2), 355–358.

RIAZ, A., HESSE, M., TCHELEPI, H.A. & ORR, F.M. 2006 Onset of convection in a gravitationally unstable diffusive boundary layer in porous media. *J. Fluid Mech.* **548**, 87–111.

RUBIN, H. & ROTH, C. 1979 On the growth of instabilities in groundwater due to temperature and salinity gradients. *Adv. Water Resour.* **2**, 69–76.

SLIM, A.C. 2014 Solutal-convection regimes in a two-dimensional porous medium. *J. Fluid Mech.* **741**, 461–491.

VAN DER MEER, B. 2005 Carbon dioxide storage in natural gas reservoir. *Oil Gas Sci. Technol.* **60** (3), 527–536.

XU, X., CHEN, S. & ZHANG, D. 2006 Convective stability analysis of the long-term storage of carbon dioxide in deep saline aquifers. *Adv. Water Resour.* **29** (3), 397–407.

YANG, F., BAI, B., TANG, D., SHARI, D.-N. & DAVID, W. 2010 Characteristics of CO_2 sequestration in saline aquifers. *Petrol. Sci.* **7** (1), 83–92.